DOI:10.1002/ejic.201400128

Structural and Physical Properties of $(EDO\text{-}TTF\text{-}Cl)_2XF_6$ (X = As, Sb) — Geometrical Aspects for mono-substituted EDO-TTF (EDO-TTF = 4,5-ethylenedioxytetrathiafulvalene)

Manabu Ishikawa,* [a] Yoshiaki Nakano,[a] Mikio Uruichi,[b] Akihiro Otsuka,[a] Kyuya Yakushi,[c] and Hideki Yamochi[a]

Keywords: Conducting Materials / Substituent Effects / Crystal Engineering / Raman Spectroscopy

$(EDO\text{-}TTF\text{-}Cl)_2XF_6$ (EDO-TTF-Cl = 4-chloro-4',5'-ethylenedioxy tetrathiafulvalene, X = As, Sb) were newly prepared to examine the substituent size effect on the packing structure of the donor molecules. In these salts, the head-to-tail type donor stacking was observed. Although the AsF_6 salt was a quasi-one-dimensional dimer-Mott insulator, SbF_6 salt showed quasi-one-dimensional metallic behavior. The detailed crystal structure analyses revealed the correlation between anion size and the intermolecular slipping among donor molecules. The donor morphology, which played important role in the overlapping mode selectivity, is characterized by the magnitude and configuration of the out-of-plane substituent size.

Introduction

The functional materials related to the electronic and/or magnetic phase transition phenomena continues to attract the attention from the scientific and industrial point of views.[1] For the development of new phase transition materials in the molecular solid, it is critically important to control the molecular packing structure.[2] However in molecular materials, even the local structure around one molecule is unpredictable because of too much internal degree of freedom (translation, rotation, and deformation of the molecule) and variety of inter-molecular interactions in a crystal lattice. Therefore the systematic study is needed to understand the relationship between the molecular structure and the molecular packing in the crystal. From the view point of molecular design for the crystal structure control, study for the 4,5-ethylenedioxytetrathiafulvalene (EDO-TTF) based system is one of the most suitable candidate for the following reasons. At first, peculiar thermal and photo-induced phase transition were observed for $(EDO\text{-}TTF)_2PF_6$ [3]. In addition, a variety of molecular packing structure changes not only by the counter component selection but the chemical modification of the donor skeleton was reported.[3,4] As a minor chemical modification of the $(EDO\text{-}TTF)_2PF_6$, 4,5-etnylenedioxy-4'-methyltetrathiafulvalene ($EDO\text{-}TTF\text{-}CH_3$) afforded the crystal of $(EDO\text{-}TTF\text{-}CH_3)_2PF_6$, where the donor packing pattern was completely different from that of $(EDO\text{-}TTF)_2PF_6$.[5] The conversion of the original head-to-tail stacking into twisted head-to-head fashion indicated the effectiveness of the methyl group even it is the smallest alkyl group. To examine the effect of the smaller substituent on the donor packing structure, the cation radical salt of 4-chloro-4',5'-ethylenedioxytetrathiafulvalene (EDO-TTF-Cl) was prepared and the structure and the Raman spectra were reported for the neutral crystal and the fully oxidized salts with PF_6.[6] In the first section of this paper, the structural and physical properties for newly obtained partially oxidized salt, $(EDO\text{-}TTF\text{-}Cl)_2XF_6$ (X = As, Sb) are described. In the second section, the anion size and substituent effects on the structural features in the donor stacking column are discussed based on the analysis of geometrical parameters.

X-ray Structure and Physical Properties

The single crystals of $(EDO\text{-}TTF\text{-}Cl)_2AsF_6$ (**1**) and $EDO\text{-}TTF\text{-}Cl)_2SbF_6$ (**2**) were obtained by the electrolysis of the ethanol solution of EDO-TTF-Cl in the presence of corresponding $[(n\text{-}C_4H_9)_4N]XF_6$ (X = As, Sb) as an electrolyte. In the examined crystallization conditions (see Experimental Section), only the title compounds were always precipitated on the anode, and the fully oxidized salt was not obtained unlikely to the case of PF_6 anion.[6] The crystallographic parameters for **1** and **2** at 300 K are summarized in Table 1 (for the temperature variation, see Table S1 and Table S2). In both crystals, one whole donor molecule and a half of the anion were crystallographically unique, and these two salts were crystallographically isomorphous. The Raman spectra of **1** and **2** were recorded and analyzed as shown in Figure 1. The Raman shift of three C=C stretching modes ν_α, ν_β, and ν_γ were observed at around the middle of those for neutral and +1 charged molecules, respectively: the charge on the donor was estimated to be +0.5 at 300 K. The charge uniformity of the donor molecule was

[a] Research Center for Low Temperature and Materials Sciences, Kyoto University, Sakyo-ku, Kyoto 606-8501, Japan.
Fax: +81-75-753-4061
E-mail: m-ishikawa@kuchem.kyoto-u.ac.jp
Homepage: http://mms.ltm.kyoto-u.ac.jp/index_e.html
[b] Institute for Molecular Science, Myodaiji, Okazaki 444-8585, Japan
[c] Toyota Institute for the chemical and physics, Nagakute, Aichi 480-1192, Japan
Supporting information for this article is available on the WWW under http://www.eurjic.org/ or from the author.

preserved at 5-300 K (for the temperature dependence of the spectra of **1** and **2**, see Figure S1 and Figure S2, respectively).

Table 1. The crystallographic data of $(EDO\text{-}TTF\text{-}Cl)_2XF_6$ (**1**: X = As, **2**: X = Sb) at 300 K.

Compound	**1**	**2**
Chemical formula	$C_{16}H_{10}O_4F_6S_8Cl_2As$	$C_{16}H_{10}O_4F_6S_8Cl_2Sb$
Formula weight	782.54	829.37
Crystal system	Triclinic	Triclinic
Space group	$P\bar{1}$	$P\bar{1}$
Crystal size / mm^3	0.4×0.2×0.05	0.4×0.2×0.05
Crystal color	Black	Black
Absorption coefficient / mm^{-1}	2.203	1.921
a / Å	7.6798(7)	7.6723(8)
b / Å	7.1978(7)	7.0984(7)
c / Å	12.4205(12)	12.8208(13)
α / °	90.657(1)	87.6930(1)
β / °	75.943(1)	77.1740(1)
γ / °	99.549(1)	99.4030(1)
V / $Å^3$	656.49(11)	669.68(12)
Z	1	1
d_{calc} / g cm^{-3}	1.979	2.057
Radiation	Mo Kα	Mo Kα
$2\theta_{max}$ / °	57	58
No. of independent obs. Reflections	3019	3192
No. of reflections with $I > 2\sigma(I)$	2301	2733
No. of refined parameters	183	183
R[a]	0.0430	0.0434
$wR2$[b]	0.1201	0.1252
GooF[c]	1.039	1.026

[a] Calculated only for the reflections with $I > 2\sigma(I)$. [b] Calculated for all of the independent reflections, $W = 1/[\sigma^2 Fo^2 + (\alpha P)^2 + \beta P]$, where $P = (Fo^2 + 2Fc^2)/3$; for **1**, $\alpha = 0.0627$, $\beta = 0.5364$; for **2**, $\alpha = 0.0768$, $\beta = 0.4552$. [c] Calculated for all of the independent reflections.

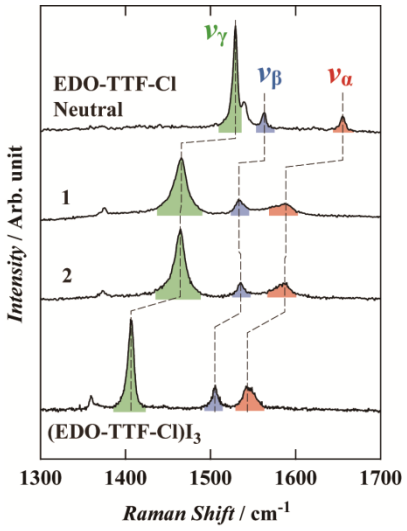

Figure 1. The comparison of the Raman spectra of $(EDO\text{-}TTF\text{-}Cl)_2XF_6$ (**1**: X = As, **2**: X = Sb) with those of neutral EDO-TTF-Cl and $(EDO\text{-}TTF\text{-}Cl)I_3$ at 300 K.

The structural feature and the physical properties of **1** are presented firstly. The *b* axis projection of the unit cells of **1** is shown in Figure 2(a). As illustrated in Figure 2(b), so-called "head-to-tail" type donor stacking column was observed along the *b* axis (for the structure of **2**, see Figure S3).

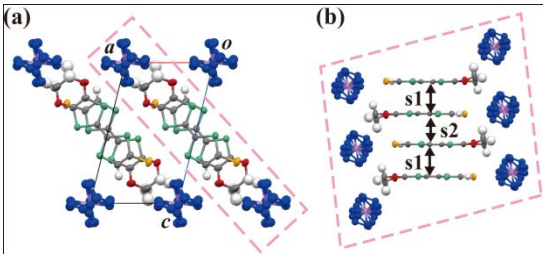

Figure 2. (a) The *b* axis projection of the crystal structure of **1** and (b) the donor short axis projection of the head-to-tail type donor stacking column at 300 K.. The areas enclosed with pink broken lines include one donor column both in (a) and (b). Two kinds of intermolecular interaction are indicated as s1 and s2. The top view of the overlap s1 and s2 are shown in Figure 3(a) and (b), respectively.

Two overlapping modes s1 and s2 were alternately appeared along the head-to-tail column. The s1 overlap (Figure 3(a)) was so-called "ring-over-atom" type which shows distinct inter molecular slipping along the donor short axis (short axis slip). The s2 overlap (Figure 3(b)) was a "ring-over-bond" type fashion with the slipping mostly along the donor long axis (long axis slip).

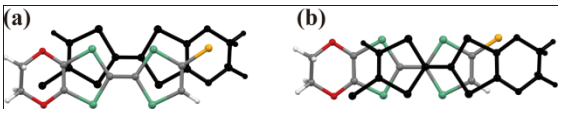

Figure 3. Two overlapping modes in **1**: (a) s1 and (b) s2. One of the two molecules is coloured by black.

The definition of overlap integrals for the extended Hückel calculation[7] are depicted in Figure 4(a). At 300 K, intra-columnar interactions s1(As) = 10.3×10^{-3} and s2(As) = 22.9×10^{-3}, while the largest inter-columnar interaction p1(As) = 8.7×10^{-3}. As the result of the competition between s1 and p1, quasi-one-dimensional Fermi surface with large warping opened along [1 0 0] was obtained as in Figure 4(b). As shown in Table S4 and Figure S4, the magnitude of p1 overlap was larger than that of s1 interaction below 200 K and the Fermi surface was opened along [1 -1 0].

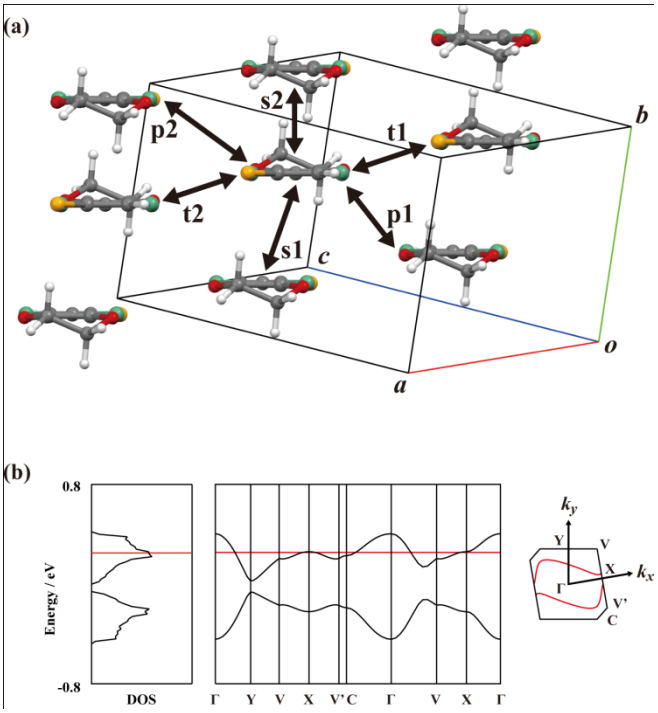

Figure 4. (a) The definition of the overlap integrals and (b) the band structure of **1** with the fermi surface at 300 K.

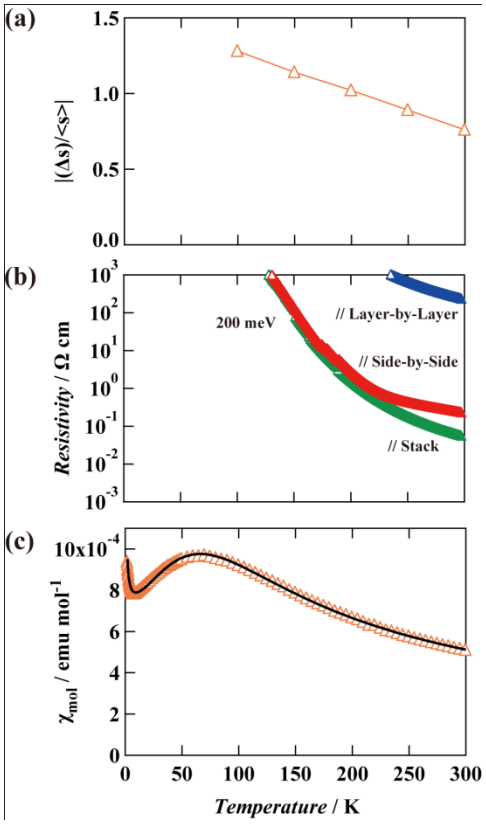

Figure 5. (a) The temperature dependence of degree of dimerization, (b) electrical resistivity, and (c) magnetic susceptibility for randomly orientated multi crystals of **1**. The crystallographic description for the current direction in (b) is given in Experimental Section.

The obtained effective half-filled band structure suggested the dimer Mott insulating state. As shown in Fig. 5(a), the degree of dimerization in the column, $|(\Delta s)/\langle s\rangle| = |2(|s1| - |s2|)/(|s1| + |s2|)|$[8] was monotonically increased with decreasing temperature. The temperature dependence of the electrical resistivity plotted in Figure 5(b) indicated nearly two-dimensional semiconducting nature in the *ab* plane at 300 K. The isotropic resistivity with activation energy of ~200 meV below 200 K supported the dominant contribution of diagonal p1 interaction (see Table S4). The magnetic susceptibility shown in Figure 5(c) was fitted by Bonner-Fisher model[9] ($N_A g^2 \mu_B^2 / k_B \sim 0.73$: 48%, $J/k_B \sim 54$ K, Curie component of ~0.2% for the formula unit), which represents the uniform one-dimensional spin array with antiferromagnetic interaction. The ratio of the spin density per formula unit was almost the half of the completely localized spin system, as observed in the other organic conductors.[10] Thus the physical properties agreed with the calculated band structure.

In the next, the results of **2** are considered (for the crystal structure of **2** at 300 K, see Figure S3). The two intra-column overlapping modes s1 and s2 for **2** are illustrated in Figure 6(a) and (b), respectively. In contrast to those in **1**, both s1 and s2 were the ring-over-bond type overlap. The magnitude of the intra-column π-π interactions (overlap integrals) at 300 K were calculated as s1(Sb) = 22.7×10^{-3} and s2(Sb) = 21.2×10^{-3}, while the largest inter-column one was p1(Sb) = 6.7×10^{-3}. The obtained band structure which is depicted in Figure 6(c) predicted the quasi-one-dimensional metallic state along the donor stack.

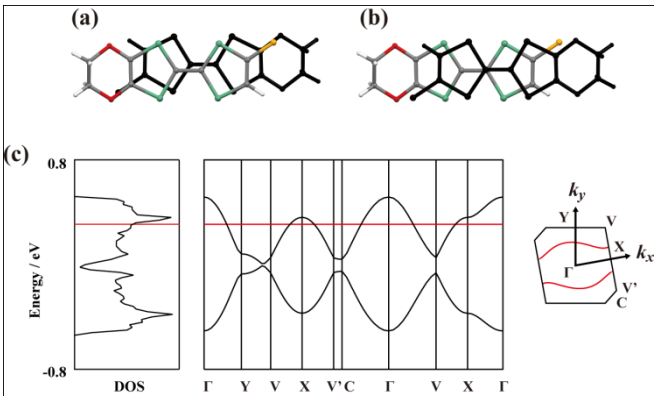

Figure 6. Two overlapping modes in **2** at 300 K: (a) s1 and (b) s2. One of the two molecules is coloured by black. (c) the band structure of **2** with the Fermi surface at 300 K.

As plotted in Figure 7(a), the degree of the dimerization was one order of magnitude smaller than that in **1**, which supported metallic behaviour in the electrical resistivity of **2** shown in Figure 7(b). The degree of dimerization exhibited a minimum at 200 K, where the crystal of **2** was always cleaved during the resistivity measurement along the donor stack. The resistivities along the side-by-side and the layer-by-layer showed broad minimum at 190 K and 140 K, respectively. Since the estimated activation energy for the semiconducting regions were ~10 meV, the activation energy along the donor stacking axis was expected to be small as well. The magnetic susceptibility shown in Figure 7(c) exhibited small and almost constant value (~3.0×10^{-4} emu mol^{-1}) above 30 K, which also agrees with the highly conducting state of **2**. Considering the HOMO band which was almost split into upper and lower Hubbard bands, the slight enhancement of the intra-column dimerization below 200 K suggested the manifestation of the dimer Mott insulating state. So far, the typical feature of further magnetic ordering such as spin density wave state[11] (saturation in the resistivity and drop in the susceptibility at the lowest temperature) was not detected apparently, as shown in Figure 7(b), (c).

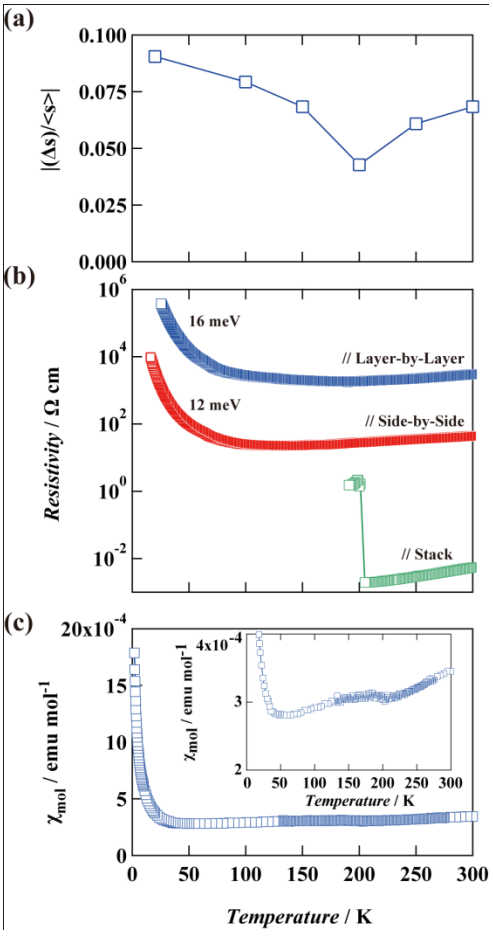

Figure 7. (a) The temperature dependence of the degree of dimerization, (b) the electrical resistivity, and (c) the magnetic susceptibility for randomly orientated multi crystals of **2** (inset: the behaviour around $\chi_{mol} = 3.0\times10^{-4}$). The crystallographic description for the current direction in (b) is given in Experimental Section.

Detailed crystal Structure Analysis

Anion Size Effect on the Donor Packing

As described above, the structural and the physical properties of **1** and **2** showed distinct difference although they were isostructural crystals. It is important to clarify the mechanism how the anion size make effect on the properties of **1** and **2**. Here, the anion size effect on the intermolecular displacements in the donor stacking column for $(EDO\text{-}TTF\text{-}Cl)_2XF_6$ is examined, since the inter-molecular slipping largely affects on the magnitude of the overlap integrals and the degree of dimerization in the donor layer.[12] Before mentioning about the intermolecular spacing, the packing freedom of the constituent molecules should be emphasized. In the observed triclinic space group with inversion symmetry, all the cell parameters are the independent free variables. Therefore, in the stuructural modulation such as anion exchange or temperature variation, molecules in the unit cell can change their relative arrangement freely, even though the inversion symmetry exists. Hence, the comparison of the general geometrical parameters, which is obtained from the relative arrangement among the donor molecules, are needed to evaluate the accurate chemical substitution effect (replacement of X = As, Sb). As depicted in Figure 3(a) and Figure 6(a), the difference in s1 overlaps indicates the freedom of the packing as mentioned above, while the similarity in s2 modes which is shown in Figure 3(b) and Figure 6(b) implies the manifestation of the strong inter-molecular attraction force. At the first stage of the discussion, the procedure to determine the “building block” in the lattice is presented.

Searching for the building block, the magnitude of the in-plane slip distance between central $S_2C{=}CS_2$ cores along the donor short and long axis (d_{short} and d_{long}, respectively) are calculated as illustrated in Figure 8(a) (see Figure S7 for the details). All of the slips for s2 mode showed temperature variation smaller than 0.1 Å, while s1 exhibited larger temperature dependence than 0.3 Å at 100-350 K (Figure S8(a) and (b)). Since the inter-planar distance between neighbouring $S_2C{=}CS_2$ cores ($d_{interplanar}$) also showed smaller temperature dependence than 0.1 Å (Figure S8(c)), the donor pair with s2 overlap (s2 dimer) is regarded as the structural building block. In other words, the temperature variation of the physical properties of **1** and **2** are mostly dominated by the change in s1 overlap. It is noticeable that the magnitude of overlap integral for s1 mode in **1** was smaller than that for s2 mode, while the absolute value of s1 in **2** was rather larger than that of s2. Therefore in **1** and **2** the magnitude of the π-π interaction is not dominant in determining the structural building block.

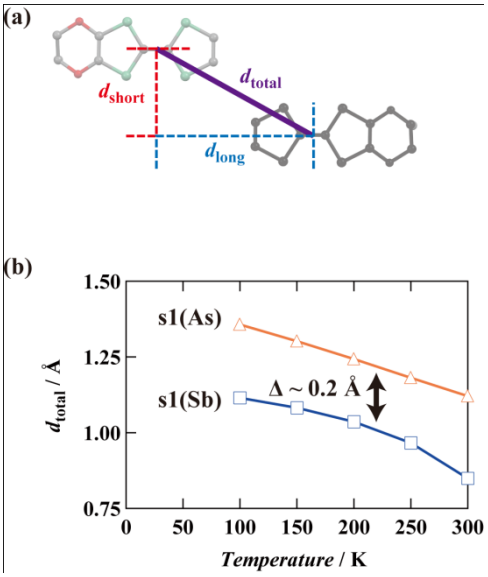

Figure 8. (a) The schematic representation of the in-plane inter-planar displacements for neighbouring donor molecules in the donor plane projection and (b) the temperature dependence of the total in-plane intermolecular displacement d_{total} for s1 in **1** and **2**.

In the next, how the anion size effect can be evaluated from the spacing between building blocks is described. For the comparison of s1 modes with different slip directions, the magnitude of the total in-plane displacements, $d_{total} = \{(d_{short})^2 + (d_{long})^2\}^{1/2}$ (Figure 8(a)) was calculated for **1** and **2**. The temperature dependence of d_{total} for s1 mode in **1** and **2** are plotted in Figure 8(b). The difference in d_{total} at each temperature was about 0.2 Å, and the d_{total} was always larger for the salt with smaller AsF_6 anion. This difference was focused as the manifestation of the chemical substitution effect (chemical pressure). To distinguish whether this anion size effect is compressive or expansive, other geometrical parameters in the donor stack, which are correlating to the magnitude of the d_{total}, are explored. As depicted in Figure 9(a), a stacking column with perfectly overlapped building blocks is assumed, where both the short and long axis slip between the neighbouring building blocks (d_{short}^{BB} and d_{long}^{BB}, respectively) are zero; the building block can be constituted by single molecule, a geometrically stable dimer, trimer, and so on. Under this perfectly overlapped condition, the distance between the gravimetric centers of neighbouring blocks (b) and the stacking periodicity between neighbouring building blocks (d_{period}) are equal and denoted as b^0 and d_{period}^0, respectively. For the dimerized system such as **1** and **2**, d_{period} is determined by the sum of two successive interplanar distances for the neighbouring donor molecules, ($d_{2success}$). The compression along the stacking direction (Figure 9(b)) causes the decrease of the b and d_{period} at the same time. While the pressure is applied along the stacking normal direction (Figure 9(c)), the column thickness is reduced to result in the in-plane displacements (d_{long}^{BB} and/or d_{short}^{BB}), in other words, the tilt angle of the building block relative to the stacking axis. In this case, the value of b must be larger than b^0 when d_{period}^0 is preserved, since b is given by $\{(d_{period}^0)^2 + (d_{short}^{BB} \text{ or } d_{long}^{BB})^2\}^{1/2}$. In the actual structures, both long and short axis slip (d_{short}^{BB} and d_{long}^{BB}) may contribute to the relaxation of the compression due to the packing freedom. Applying this model to **1** and **2**, the b and d_{period} ($d_{2success}$) at 300 K were calculated and summarized in Table 2 with d_{total}. Compared to the values in **2**, the larger b and the smaller d_{period} in **1** are corresponding to the compression along the normal and parallel to the stacking direction, respectively. The larger d_{total} in **1** also agrees with this tendency.

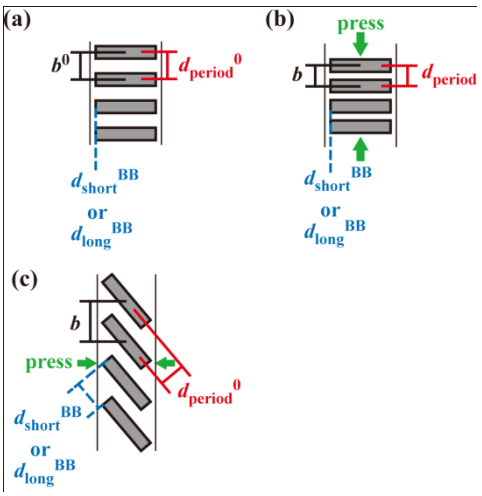

Figure 9. The schematic illustration of the pressure effect on the donor stacking structure from the donor long or short axis projection. The grey rectangles represent the building block. Two vertical lines beside the stack are the guide for the column thickness. (a) the column with perfectly overlapped building blocks, where $b^0 = d_{period}^0$, d_{short}^{BB} or $d_{long}^{BB} = 0$, (b) the effect of the uniaxial strain along the stacking direction, where $b^0 > b = d_{period}^0$, d_{short}^{BB} or $d_{long}^{BB} = 0$, (c) the effect of the horizontal compression to the stacking depicted in (a), where $b > b^0 = d_{period}^0$, and d_{short}^{BB} or $d_{long}^{BB} = 0$.

Table 2. The inter-building-block spacing for $(EDO\text{-}TTF\text{-}Cl)_2XF_6$ at 300 K.

Compound	X	b / Å	d_{period} / Å ($d_{2success}$)	d_{total} / Å
1	As	7.20	7.03	1.12
2	Sb	7.10	7.08	0.85

The evaluated chemical pressure effect based on the donor packing geometry is also supported by the relative anion size to the building block (s2 dimer) in **1** and **2**. The anion size along the donor short and long axes and the donor plane normal direction (W_A, L_A , and T_A, respectively) are measured on the space filling model in the projection image along the donor plane normal direction and the adonor short axis (Figure 10). The sizes for the s2 dimer (W_{s2}, L_{s2}, and T_{s2}, respectively) which were measured correspondingly to W_A, L_A , and T_A are summarized in Table 3.

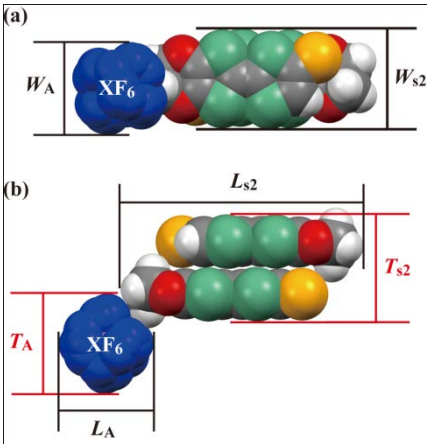

Figure 10. The definition of the molecular sizes in the (a) donor plane normal and (b) donor short axis projection.

Table 3. The molecular size and size ratio between the anion and s2 dimer in $(EDO\text{-}TTF\text{-}Cl)_2XF_6$ at 300 K.

Compound	**1**	**2**
(W_A/ Å)/(W_{s2}/ Å)	(6.00)/(6.63) = 0.90	(6.08)/(6.60) = 0.92
(L_A/ Å)/(L_{s2}/ Å)	(5.84)/(16.12) = 0.36	(6.40)/(16.36) = 0.39
(T_A/ Å)/(T_{s2}/ Å)	(6.29)/(7.04) = 0.89	(6.65)/(7.11) = 0.94

The values of W_A, L_A , and T_A, and their ratio with W_{s2}, L_{s2}, and T_{s2}, respectively, are all smaller in **1** than those observed in **2**. Then the compressive reconstruction of the molecular arrangement by changing SbF_6 to AsF_6 was attributed to the actual anion shrinking along three directions. Therefore the chemical pressure effect in the isomorphous crystals **1** and **2** was successfully evaluated by the geometrical parameters calculated from the donor packing as modeled in Figure 9. At the same time, the physical properties of the two, which is explained by the degree of intra-columnar dimerization, were also well explained by the chemical pressure originated from the anion size. The procedure described above will be a general method to evaluate the actual counter component size effect, especially in the materials with planar molecular skeleton. The effectiveness of the procedure should be examined in other systems.

Here, it is notable that all the effective anion sizes are smaller than the size of s2 dimer, despite the maximum diameter of SbF_6 (6.68 Å, estimated from the observed Sb-F lengths and the van der Waals (vdW) radius[13] of F atom) is larger than the width of s2 dimer (6.60 Å, obtained from S to S distance in the same 1,3-dithiol ring, the vdW radius of S atom, and d_{short} for s2 dimer). Thus in the crystal structure design, the counter ion should be selected regarding the rotational freedom as well as the maximum diameter. The consideration of smaller and larger counter anions than AsF_6 and SbF_6, respectively, are needed to lead the drastic donor packing pattern change by the anion size effect.

Substituent Size Effect on the Donor Packing

The effect of the substituent R on the crystal structure is examined. As seen in Figure 6 and Figure 11, the donor stacking fashions in **2** were fundamentally similar to those observed in $(EDO\text{-}TTF)_2SbF_6$ (**3**) except for the direction of the long axis slip for s1, as summarized in Table 4.

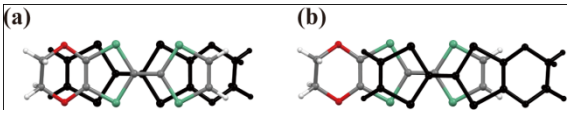

Figure 11. Two overlapping modes in **3**: (a) s1 and (b) s2. One of the two molecules is coloured by black.

Table 4. The intra-column displacements for $(EDO\text{-}TTF\text{-}R)_2SbF_6$ at 300 K.

Compound	R	d_{short} (s1)	d_{long} (s1)	d_{short} (s2)	d_{long} (s2)
2	Cl	0.33	0.78	0.04	1.26
3	H	0.00	-0.92	0.14	1.02

To understand the differences in the parameters listed in Table 4, the size of substituent R is focused. The chemical structure and the sizes of substituent R for currently obtained EDO-TTF derivatives are shown in Scheme 1.

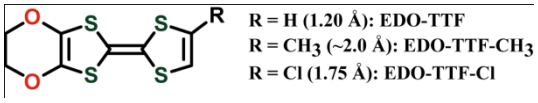

Scheme 1. The chemical structure of EDO-TTF and its mono-substituted derivatives. The size of each substituent R given in parentheses are based on Bondi's vdW radii[13]. The size of methyl group was evaluated based on the observed geometry and of vdW radius of hydrogen.

The lengths of the donors shown in Scheme 1 were measured in the picture image of the donor plane projection in space-filling representation (Figure 12). The lengths of EDO-TTF, EDO-TTF-CH_3, and EDO-TTF-Cl were estimated to be ~12.7 Å, ~13.7 Å, and ~14.0 Å, respectively. The largest donor length for intermediate substituent size is resulted from the total effect of the substituent on the molecular geometry (difference in substituent size and change in the bond lengths and angles). The effective out-of-TTF-plane bulkiness of each substituent was defined as the size difference from the sulphur atom (1.80 Å). Ethylenedioxy group, the common bulky substituent for the three donors, exhibited flexibility of the hump from 0.2 to 1.2 Å depending on the ethylene conformation and the bending of the 1,3-dithiol ring (Figure S9). On the other hand, the size of the substituent R at the vinyl position (vinyl-R) show the fixed relative size to the sulphur atom: the hydrogen (-0.60 Å: considerably smaller), the chlorine (-0.05 Å: very similar), and the methyl group (~+0.2 Å: larger) relative to the sulphur atom, respectively.

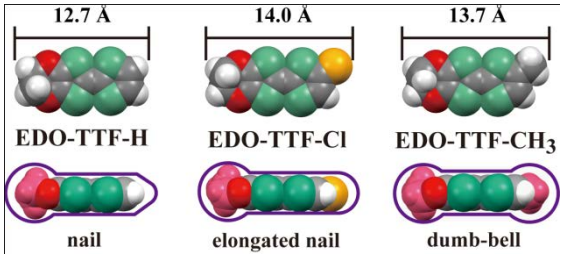

Figure 12. The donor plane normal and short axis projection for EDO-TTF-R in the space-filling model (top and bottom, respectively). In the donor short axis projection, the bulky substituent than sulphur atom are coloured by magenta. Purple line: the guide for eye to emphasize the morphology of each π-donor molecule.

The stacking feature in **2** and **3**, which formed head-to-tail type columns are compared to examine the substituent effect of vinyl-R. As seen in Figure 13(a), the hollows at the upper and lower side of vinyl-hydrogen for **3** accommodate the out-of-plane protrusion of the axial ethylene-hydrogen in the neighbouring molecules. The amount of the out-of-plane hump for s1 side (upper donor pair) at 300 K was ~0.30 Å, which can be completely accepted by the hollow at the vinyl-hydrogen (−0.6 Å): the collision of the hump of axial ethylene-hydrogen at s1 side can only occur against vinyl-carbon. In contrast, in Figure 13(b), the hollow depth around the chlorine is too small to accommodate the neighbouring ethylene hump, and it is apparent that the position of the vinyl carbon in the s1 side of **3** is occupied by the vinyl-Cl at s1 overlap (upper pair). For the s2 side of **3** (lower pair) in Figure 13(a), the ethylene hump was estimated to be 1.2 Å. The difference in the magnitude of axial ethylene hump between s1 and s2 side in **3** is originated from the bending freedom of the 1,3-dithiol ring with ethylenedioxy group (dihedral angle between vinyl S-C=C-S plane at the side of ethylenedioxy group and $S_2C=CS_2$ TTF core plane in the TTF skeleton was ~6.0˚). The smaller bent angle of 1,3-dithiol ring (~1.6˚) observed in **2** also supports the correspondence between the bent angle and the hollow depth in s2 side. The difference in the in-plane displacement in the head-to-tail stacking columns in **2** and **3** was well corresponded to the hump at ethylenedioxy group and the hollow at vinyl-R.

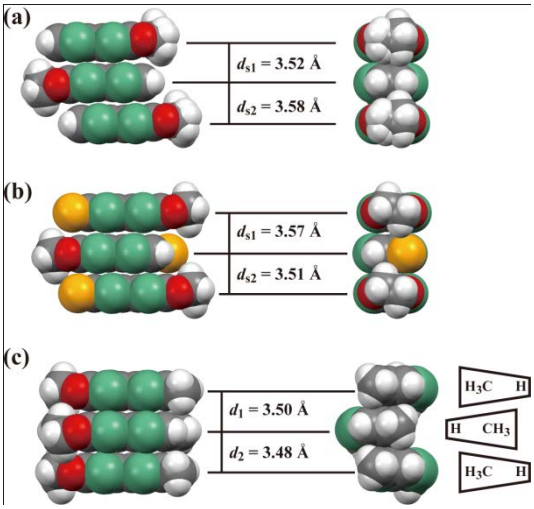

Figure 13. (a) The donor stacking column viewed along the donor short and long axes, left and right, respectively (a) in **3** at 300 K, (b) in **2** at 300 K, and (c) in $(EDO\text{-}TTF\text{-}CH_3)_2PF_6$ at 290 K depicted in the space-filling model.

On the other hand, based on the donor side view morphology shown in Figure 12, it was found that EDO-TTF-CH_3 has different steric feature due to the out-of-plane bulkiness of the methyl group. The morphology of the EDO-TTF and EDO-TTF-Cl in their short axis projection are categorized as the "nail" and "half-elongated nail", while the EDO-TTF-CH_3 is classified as "half-elongated dumb-bell". In Figure 13(c), a zig-zag orientation of the methyl group was observed along the twisted head-to-head column of EDO-TTF-CH_3.[5] This indicated the importance of the "dumb-bell" shape, since it is clear that the two dumb-bells are required to be twisted to make contact between the grips. The $d_{2success}$ in $(EDO\text{-}TTF\text{-}CH_3)_2PF_6$ at 290 K was 6.98 Å, which is considerably smaller than the values summarized in Table 2. The smaller $d_{2success}$ instead of the largest vinyl-R suggests the manifestation of the key and key-hole effect between the neighbouring EDO-TTF-CH_3's. The averaged overlap integrals observed in the stacking columns are approximately ~27×10^{-3}, ~22×10^{-3}, and ~5×10^{-3} for **3**, **2**, and $(EDO\text{-}TTF\text{-}CH_3)_2PF_6$, respectively. The reduced π-π interaction in the twisted column of EDO-TTF-CH_3 in spite of the smaller $d_{2success}$ also supports the predominance of the steric effect between the bulky substituents. Thus, it was found that the geometry in the donor overlapping mode in EDO-TTF-R system is very correlated with the size of vinyl-R, which characterize the donor morphology based on the magnitude and the configuration of the humps and hollows. This type of categorization is expected to open the new way for the molecular design based crystal structure control.

Conclusions

The substituent effect on the structural and the physical properties of $(EDO\text{-}TTF\text{-}R)_2XF_6$ (X = As, Sb) was examined. As the smaller substituent than the methyl group, chlorine atom was utilized as vinyl-R. The head-to-tail type stacking observed in the pristine $(EDO\text{-}TTF)_2XF_6$ was successfully retained in the analogous salts of EDO-TTF-Cl. The electronic structure of **1** and **2** were both quasi-one dimensional and dominated by the magnitude of the degree of the intra-columnar dimerization.

As the detailed crystal structure analysis, the method to determine the building block in the crystal and the way to evaluate the chemical pressure effect on the inter-building block spacing were demonstrated, which revealed that the stronger dimerization observed in **1** is originating from the compression of the donor packing space by the smaller anion size. Furthermore, the donor substituent size effect was evaluated from the magnitude of the humps and hollows relative to the thickness of the TTF plane. The origin of the difference in the magnitude of the long axis slip between **2** and **3** were attributed to the smaller hollow depth around the chlorine than the vinyl-hydrogen. The categorization of the donor shape is newly proposed based on the donor morphology in the short axis projection, which well explains the donor packing pattern observed in the 2:1 salts of EDO-TTF-R with octahedral anions.

The concept of molecular shape categorization based on the magnitude and the configuration relative to the main skeleton will be applicable to TTF analogues and other π-conjugated molecules. The exploration of the new functional materials and the consideration of the crystal structure in this context will be continued to establish more general guidelines for the molecular shape based crystal engineering.

Experimental Section

For the electrocrystalliation of title compounds, the electrolytes $[(n\text{-}C_4H_9)_4N]XF_6$ (X = As, Sb) was recrystallized from the appropriate solvents. As the solvent, ethanol was distilled from Mg/I_2 and stored under argon atmosphere. In an H-shaped cell with a glass frit separating two compartments, EDO-TTF-Cl and electrolyte were placed in the anodic and both chambers, respectively. After dissolving the donor and supporting electrolyte under argon, a constant current was applied between the platinum electrodes of the diameters of 2 and 1 mm for the anode and cathode, respectively. In a typical procedure, the donor (ca. 12 mg) and supporting electrolyte (ca. 40 mg) were dissolved in 18 mL of EtOH. The electro-oxidation applying 0.5 μA for 1 week afforded the radical cation salts as black elongated plates. The other crystallization conditions examined: the magnitude of a current (0.5-8.0 μA), temperature (at 5-30 °C).

The X-ray diffraction images were collected by the Bruker SMART ApexII CCD. The graphite monochromated MoKα radiation by 50 kV, 30 mA was irradiated to the single crystal sample. The measurement temperature was controlled with a Japan Thermal Engineering Co. Ltd. cooling system DX-CS190LD. The structure was solved by the direct method SIR2004[14] and refined with a full-matrix least-squares method against F^2 using SHELX-97[15] utilizing Yadokari-XG program.[16] The position of the hydrogen atom was calculated geometrically and refined by the riding model with U_{iso} = 1.2 U_{eq} of the connected carbon atom. Each C-H length was fixed to 1 Å. The X-ray diffraction for **2** at ~20 K was carried out utilizing Rigaku 4176F07. The sample temperature under helium gas flow was controled with a Japan Thermal Engeneering Co., Ltd. XR-HR10K .

The Raman spectra were recorded by Renishaw inVia Reflex spectrometer at 5-300 K in 180° back-scattering geometry. The sample in the Oxford Microstat cryostat was irradiated by a polarized 633 nm laser of 0.04 mW to avoid the sample damage. The maximum intensity of the Raman scattering was achieved by the polarization along the donor long axis.

The electrical resistivity measurement was performed along the crystal long, wide, and thick directions. For **1**, the long, wide, and thick directions were parallel to [0 1 0], [1 0 −1], and [1 0 1], respectively, while for **2**, those were parallel to [0 1 0], [1 0 1], and [1 0 −1], respectively. The standard four-probe method was utilized for long and wide directions, and parallel four-probe method, where the pair of the current and voltage probes were attached on the crystal surfaces in parallel, was applied for the thickness direction. The Au wires (φ 10 μm) were fixed on the crystal surface by carbon paste (JEOL Dotite).

The magnetic susceptibility was recorded by Quantum Design MPMS SQUID susceptometer. The susceptibility of randomly oriented polycrystalline samples were measured under the magnetic field of 0.5 T. The diamagnetic core correction was performed based on the Pascal's law.

Supporting Information (see footnote on the first page of this article): CCDC-984320, CCDC-984321 to 984326, CCDC-984328 to 984334 contains the supplementary crystallographic data for this paper. These data can be obtained free of charge from The Cambridge Crystallographic Data Centre via www.ccdc.cam.ac.uk/data_request/cif. The CIF files for the crystal structure of **1** at 100-350 K (CCDC-984321 to 984326), **2** at 20-350 K (CCDC-984328 to 984334), and **3** at 300 K (CCDC-984320) are available. The temperature variation of crystallographic parameters, Raman spectra, and the result of the extended Hückel calculation are provided together with the details of the crystal structure analysis.

Acknowledgments

M. I. thanks Mr. Y. Okano (Institute for Molecular Science Instrument Center) for the X-ray measurement of **2** at 20 K and Y. N. is indebted to the Chubei Itoh Foundation. This work was in part supported by a Grant-in-Aid for Scientific Research on Innovative Areas (20110006) and (23225005) from the Ministry of Education, Culture, Sports, Science and Technology (MEXT), Japan and for Creative Scientific Research (18GS0208) from JSPS and by the Joint Studies Program (2009-2011) of the Institute for Molecular Science, Nanotechnology Platform Program (Molecule and Material Synthesis) of the Ministry of Education, Culture, Sports, Science and Technology (MEXT), Japan.

[1] (a) G. Saito and Y. Yoshida, *Bull. Chem. Soc. Jpn.*, **2007**, *80*, 1-137. (b) N. Martin, *Chem. Comn.*, **2013**, *49*, 7025-7027.

[2] (a) T. Mori, *Bull. Chem. Soc. Jpn.*, **1998**, *71*, 2509-2526. (b) T. Mori, *Bull. Chem. Soc. Jpn.*, **1999**, *71*, 2011-2027. (c) T. Mori, *Bull. Chem. Soc. Jpn.*, **1999**, *72*, 179-197.

[3] H. Yamochi and S. Koshihara, *Sci. Technol. Adv. Mater.*, **2009**, *10*, 024305.

[4] (a) Y. Nakano, H. Yamochi, G. Saito, M. Uruichi, and K. Yakushi, *J. Phys., Conf. Ser.*, **2009**, *148*, 012007. (b) A. Ota, H. Yamochi, and G. Saito, *J. Low Temp. Phys.*, **2006**, *142*, 425-428. (c) A. Ota, H. Yamochi, and G. Saito in *Multifunctional Conducting Molecular Materials* (Eds.: G. Saito, F. Wudl, R.C. Haddon, K. Tanigaki, T. Enoki, H.E. Katz, M. Maesato), RSC Publishing, Cambridge, UK., **2007**, pp. 115-118.

[5] X. F. Shao,Y. Yoshida, Y. Nakano, H. Yamochi, M. Sakata, M. Maesato, A. Otsuka, G. Saito, and S. Koshihara, *Chem. Mater.*, **2009**, *21*, 1085-1095.

[6] M. Ishikawa, Y. Nakano, M. Uruichi, K. Yakushi, and H. Yamochi., *Phys. stasus solidi C*, **2012**, *9*, 1143-1145.

[7] (a) R. H. Summerville and R. Hoffman, *J. Am. Chem. Soc.*, **1976**, *98*, 7240-7254. (b) M. M. L. Chen and R. Hoffman, *J. Am. Chem. Soc.*, 1976, *98*, 1647-1653.

[8] J.P. Pouget and S. Ravy, *J. Phys. I France*, **1996**, *6*, 1501-1525.

[9] W. E. Hatfield, R. R. Welleer, and J. W. Hall, *Inorg. Chem.*, **1980**, *19*, 3825-3828.

[10] (a) H. Mori, T. Okano, S. Tanaka, M. Tamura, Y. Nishio, K. Kajita, and T. Mori, *J. Phys. Soc. Jpn.*, **2000**, *69*, 1751-1756. (b) H. Nishikawa, Y. Sato, K. Kikuchi, T. Kodama, I. Ikemoto, J. Yamada, H. Oshio, R. Kondo, and S. Kagoshima, *Phys. Rev. B*, **2005**, *72*, 052510. (c) M. Noda, M. Yasuda, Y. Nakano, A. Ito, H. Fueno, K. Tanaka, H. Fujiwara, T. Sugimoto, and Y. Misaki, Chem. Lett., **2008**, *37*, 396-397.

[11] (a) T. Mori and H. Inokuchi, *Solid State Comun.*, **1989**, *70*, 823-827. (b) T. Nakamura, *J. Phys. Soc. Jpn.*, **2000**, *69*, 4026-4033.

[12] (a) T. Mori, *Bull. Chem. Soc. Jpn.*, **1984**, *57*, 627-633. (b) T. Mori, *Bull. Chem. Soc. Jpn.*, **1998**, *71*, 2509-2526.

[13] A. Bondi, *J. Phys. Chem.*, **1964**, *68*, 441-451.

[14] M. C. Burla, R. Caliandro, M. Camalli, B. Carrozzini, G. L. Cascarano, L. De Caro, C. Giacovazzo, G. Polidori, and R. Spagna, *J. Appl. Cryst.*, **2005**, *38*, 381-388.

[15] G. M. Sheldrick, *Acta Cryst A* **2008**, *64*, 112-122.

[16] Yadokari-XG, Software for Crystal Structure Analyses, K. Wakita (2001); Release of Software (Yadokari-XG 2009) for Crystal Structure Analyses, C. Kabuto, S. Akine, T. Nemoto, and E. Kwon, J. Cryst. Soc. Jpn., **2009**, *51*, 218-224.

Received: January 30, 2014
Published online: April 24, 2014

Entry for the Table of Contents

Key Topic

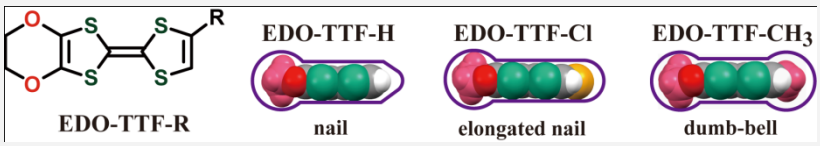

Keywords: Conducting Materials / Substituent Effects / Crystal Engineering / Raman Spectroscopy

The secimonducting and metallic $(EDO\text{-}TTF\text{-}Cl)_2XF_6$ (X = As, Sb, respectively) were newly obtained. The properties are well correlated with the intra-columnar degree of the dimerization. The geometrical analyses demonstrated the importance of the rotational freedom in the anion size evaluation.

The in-plane intermolecular displacements in the donor stacking columns are the key parameters to understand the chemical pressure. The correlation between the donor shape in its short axis projection and the donor stacking fashion is elucidated.

Supporting Information

Table S1 Crystallographic parameters for $(EDO\text{-}TTF\text{-}Cl)_2AsF_6$ (1) at 100-350 K.

Temperature / K	**100**	**150**	**200**	**250**	**350**
Chemical formula	$C_{16}H_{10}O_4F_6S_8Cl_2As$	$C_{16}H_{10}O_4F_6S_8Cl_2As$	$C_{16}H_{10}O_4F_6S_8Cl_2As$	$C_{16}H_{10}O_4F_6S_8Cl_2As$	$C_{16}H_{10}O_4F_6S_8Cl_2As$
Formula weight	782.54	782.54	782.54	782.54	782.54
Crystal system	Triclinic	Triclinic	Triclinic	Triclinic	Triclinic
Space group	$P\bar{1}$	$P\bar{1}$	$P\bar{1}$	$P\bar{1}$	$P\bar{1}$
Crystal size / mm^3	0.4×0.2×0.05	0.4×0.2×0.05	0.4×0.2×0.05	0.4×0.2×0.05	0.4×0.2×0.05
Crystal color	Black	Black	Black	Black	Black
Absorption coefficient / mm^{-1}	2.289	2.269	2.245	2.221	2.181
a / Å	7.6103(5)	7.6246(5)	7.6438(6)	7.6646(6)	7.700(2)
b / Å	7.0897(5)	7.1131(5)	7.1418(6)	7.1722(6)	7.226(2)
c / Å	12.2217(9)	12.2731(9)	12.328(1)	12.3796(9)	12.468(4)
α / °	91.582(1)	91.448(1)	91.246(1)	90.985(1)	90.258(4)
β / °	75.713(1)	75.829(1)	75.919(1)	75.948(1)	75.944(4)
γ / °	98.696(1)	99.026(1)	99.312(1)	99.475(1)	99.558(4)
V / $Å^3$	631.65(8)	637.32(8)	644.04(9)	650.98(9)	663.1(3)
Z	1	1	1	1	1
d_{calc} / g cm^{-3}	2.057	2.039	2.018	1.996	1.960
Radiation	Mo Kα	Mo Kα	Mo Kα	Mo Kα	Mo Kα
$2\theta_{max}$ / °	58	58	58	58	58
No. of independent obs. Reflections	2916	2943	2963	2998	3060
No. of reflections with $I > 2\sigma(I)$	2669	2583	2495	2437	2164
No. of refined parameters	173	183	183	183	183
R[a]	0.0305	0.0311	0.0345	0.0391	0.0468
$wR2$[b]	0.0770	0.0815	0.0927	0.1063	0.1292
GooF[c]	1.041	1.032	1.032	1.021	1.015

[a] Calculated only for the reflections with $I > 2\sigma(I)$. [b] Calculated for all of the independent reflections, $W = 1/[\sigma^2 Fo^2 + (\alpha P)^2 + \beta P]$, where $P = (Fo^2 + 2Fc^2)/3$; for 350 K, $\alpha = 0.0596$, $\beta = 0.7279$; for 250 K, $\alpha = 0.0558$, $\beta = 0.6964$; for 200 K, $\alpha = 0.0495$, $\beta = 0.593$; for 150 K, $\alpha = 0.0455$, $\beta = 0.5187$; for 100 K, $\alpha = 0.0373$, $\beta = 0.9483$. [c] Calculated for all of the independent reflections.

Table S2 Crystallographic parameters for $(EDO\text{-}TTF\text{-}Cl)_2SbF_6$ (2) at 100-350 K.

Temperature / K	**100**	**150**	**200**	**250**	**350**
Chemical formula	$C_{16}H_{10}O_4F_6S_8Cl_2Sb$	$C_{16}H_{10}O_4F_6S_8Cl_2Sb$	$C_{16}H_{10}O_4F_6S_8Cl_2Sb$	$C_{16}H_{10}O_4F_6S_8Cl_2Sb$	$C_{16}H_{10}O_4F_6S_8Cl_2Sb$
Formula weight	829.37	829.37	829.37	829.37	829.37
Crystal system	Triclinic	Triclinic	Triclinic	Triclinic	Triclinic
Space group	$P\bar{1}$	$P\bar{1}$	$P\bar{1}$	$P\bar{1}$	$P\bar{1}$
Crystal size / mm^3	0.4×0.2×0.05	0.4×0.2×0.05	0.4×0.2×0.05	0.4×0.2×0.05	0.4×0.2×0.05
Crystal color	Black	Black	Black	Black	Black
Absorption coefficient / mm^{-1}	2.005	1.987	1.967	1.944	1.899
a / Å	7.6070(7)	7.6176(8)	7.6171(10)	7.6328(8)	7.7082(9)
b / Å	6.8934(7)	6.9335(8)	6.9817(9)	7.0334(7)	7.1679(9)
c / Å	12.6398(12)	12.6862(14)	12.7884(16)	12.8464(14)	12.7957(15)
α / °	86.434(1)	86.529(1)	86.529(2)	86.834(1)	88.292(2)
β / °	79.613(1)	79.201(2)	78.412(2)	77.764(1)	76.685(2)
γ / °	98.819(1)	99.024(1)	99.567(2)	99.475(1)	99.327(1)
V / $Å^3$	641.48(11)	647.23(12)	653.85(15)	661.45(12)	677.22(14)
Z	1	1	1	1	1
d_{calc} / g cm^{-3}	2.147	2.128	2.106	2.082	2.034
Radiation	Mo Kα	Mo Kα	Mo Kα	Mo Kα	Mo Kα
$2\theta_{max}$ / °	57	58	57	57	58
No. of independent obs. Reflections	2872	2890	2924	2993	3106
No. of reflections with $I > 2\sigma(I)$	2739	2676	2653	2698	2532
No. of refined parameters	178	173	183	183	173
R[a]	0.0274	0.0297	0.0318	0.0358	0.0480
$wR2$[b]	0.0732	0.0816	0.0881	0.1030	0.1461
GooF[c]	1.041	1.052	1.034	1.051	1.035

[a] Calculated only for the reflections with $I > 2\sigma(I)$. [b] Calculated for all of the independent reflections, $W = 1/[\sigma^2 Fo^2 + (\alpha P)^2 + \beta P]$, where $P = (Fo^2 + 2Fc^2)/3$; for 350 K, $\alpha = 0.0889$, $\beta = 0.4831$; for 250 K, $\alpha = 0.0656$, $\beta = 0.4425$; for 200 K, $\alpha = 0.0544$, $\beta = 0.575$; for 150 K, $\alpha = 0.0526$, $\beta = 0.596$; for 100 K, $\alpha = 0.045$, $\beta = 0.8999$. [c] Calculated for all of the independent reflections

Table S3 Crystallographic parameters for (EDO-TTF-R)$_2$XF$_6$ at 300 K.

Compound	**R = Cl, X = As (1)**	**R = Cl, X = Sb (2)**	**R = H, X = Sb (3)**
Chemical formula	$C_{16}H_{10}O_4F_6S_8Cl_2As$	$C_{16}H_{10}O_4F_6S_8Cl_2Sb$	$C_{16}H_{12}O_4F_6S_8Sb$
Formula weight	782.54	829.37	760.49
Crystal system	Triclinic	Triclinic	Triclinic
Space group	$P\bar{1}$	$P\bar{1}$	$P\bar{1}$
Crystal size / mm^3	0.4×0.2×0.05	0.4×0.2×0.05	0.22×0.12×0.12
Crystal color	Black	Black	Black
Absorption coefficient / mm^{-1}	2.203	1.921	1.837
a / Å	7.6798(7)	7.6723(8)	7.2731(3)
b / Å	7.1978(7)	7.0984(7)	7.3599(4)
c / Å	12.4205(12)	12.8208(13)	12.2504(6)
α / °	90.657(1)	87.6930(1)	93.035(1)
β / °	75.943(1)	77.1740(1)	74.226(1)
γ / °	99.549(1)	99.4030(1)	96.985(1)
V / Å^3	656.49(11)	669.68(12)	626.24(5)
Z	1	1	1
d_{calc} / g cm^{-3}	1.979	2.057	2.017
Radiation	Mo Kα	Mo Kα	Mo Kα
$2\theta_{max}$ / °	57	58	59
No. of independent obs. Reflections	3019	3192	3173
No. of reflections with $I > 2\sigma(I)$	2301	2733	2944
No. of refined parameters	183	183	163
R[a]	0.0430	0.0434	0.0376
$wR2$[b]	0.1201	0.1252	0.1066
GooF[c]	1.039	1.026	1.058

[a] Calculated only for the reflections with $I > 2\sigma(I)$. [b] Calculated for all of the independent reflections, $W = 1/[\sigma^2 Fo^2 + (\alpha P)^2 + \beta P]$, where $P = (Fo^2 + 2Fc^2)/3$; for **1**, $\alpha = 0.0627$, $\beta = 0.5364$; for **2**, $\alpha = 0.0768$, $\beta = 0.4552$; for **3**, $\alpha = 0.061$, $\beta = 0.5571$;. [c] Calculated for all of the independent reflections.

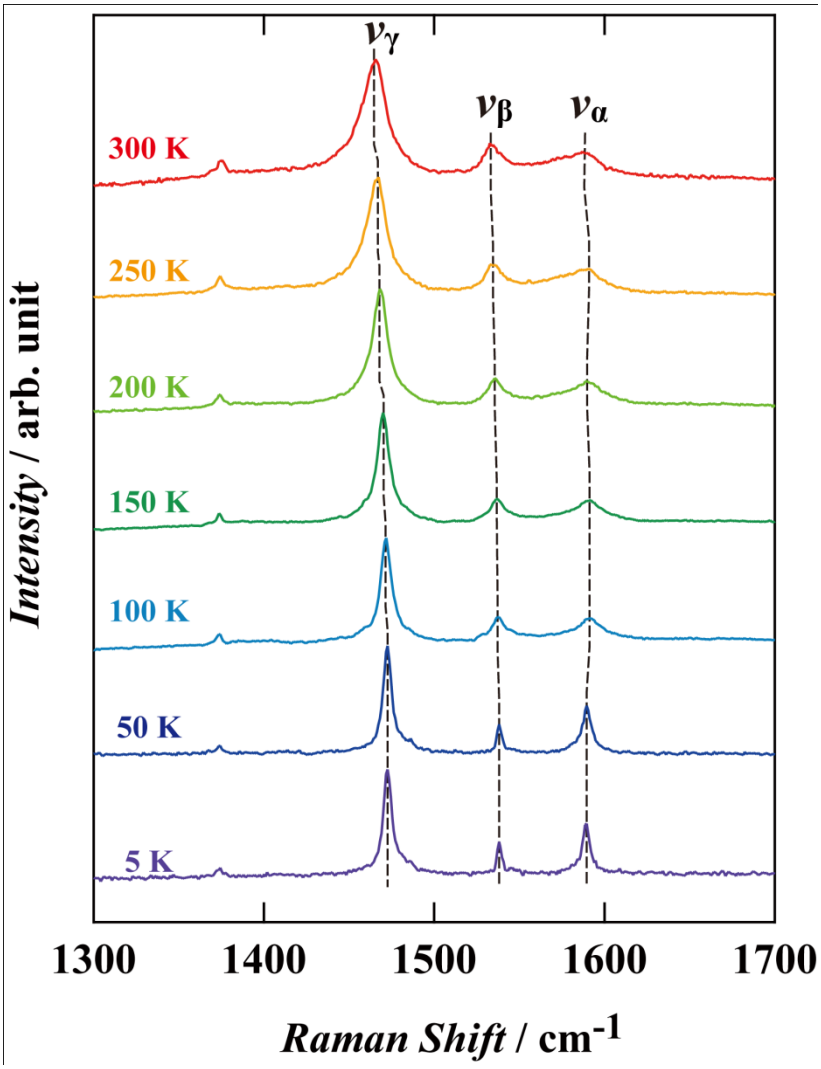

Figure S1 The temperature dependence of Raman spectra of **1**. The intensity of each spectrum was normalized for the intensity at around 1470 cm^{-1}. Only a slight shift and the sharpening of three C=C stretching modes (ν_α, ν_β, and ν_γ) indicated the preservation of the uniform oxidation state of donor molecules. The excitation wavelength was 633 nm and the laser power was 35-70 μW. The exposure time for each measurement was 30 sec times 20.

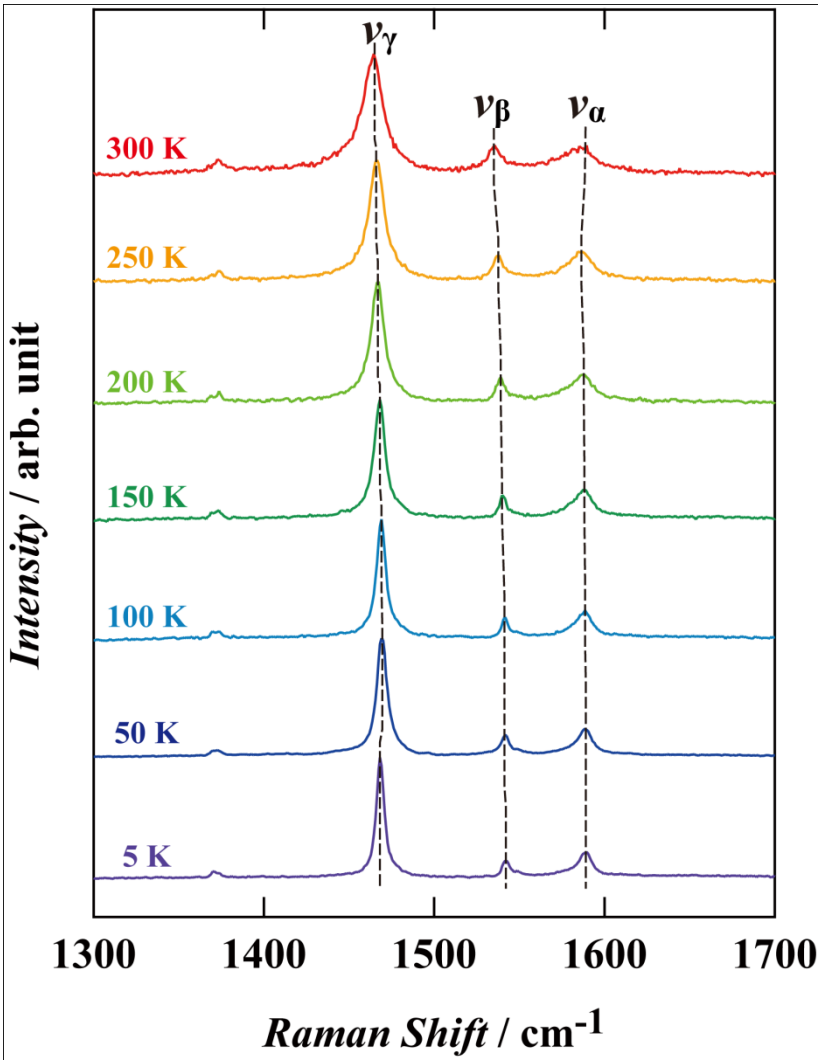

Figure S2 The temperature dependence of the Raman spectra of **2**. The intensity of each spectrum was normalized for the intensity at around 1470 cm^{-1}. Only a slight shift and the sharpening of three C=C stretching modes (ν_α, ν_β, and ν_γ) indicated the preservation of the uniform oxidation state of donor molecules. The excitation wavelength was 633 nm and the laser power was 30-35 μW. The exposure time for each measurement was 30 sec times 20-30.

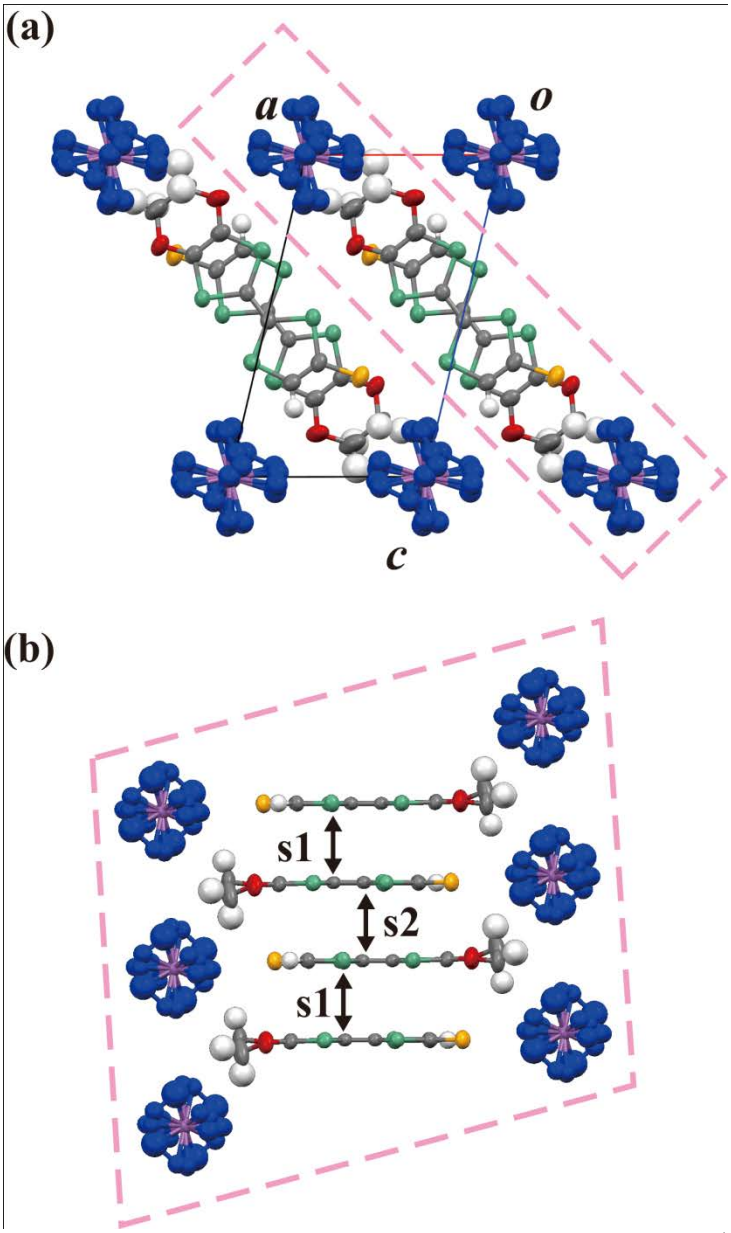

Figure S3 (a) The *b* axis projection of the crystal structure of **2** at 300 K. (b) the donor short axis projection of the head-to-tail stacking column at 300 K. In the pink broken line, one donor column is included. The overlap s1 and s2 are the two alternating modes in the donor column. The top view of the overlap s1 and s2 are shown in Figure 6(a) and (b), respectively.

Table S4. The overlap integrals of $(EDO\text{-}TTF\text{-}Cl)_2AsF_6$ (1) in the unit of 10^{-3}.

Temp.	100 K	150 K	200 K	250 K	300 K	350 K
s1	5.6	6.8	8.0	9.1	10.3	11.5
s2	25.7	24.9	24.6	23.8	22.9	22.1
t1	2.2	1.8	1.5	1.2	1.0	0.8
t2	2.2	1.8	1.5	1.2	1.0	0.8
p1	9.0	9.0	9.1	8.9	8.7	8.3
p2	0.5	0.5	0.5	0.5	0.5	0.5

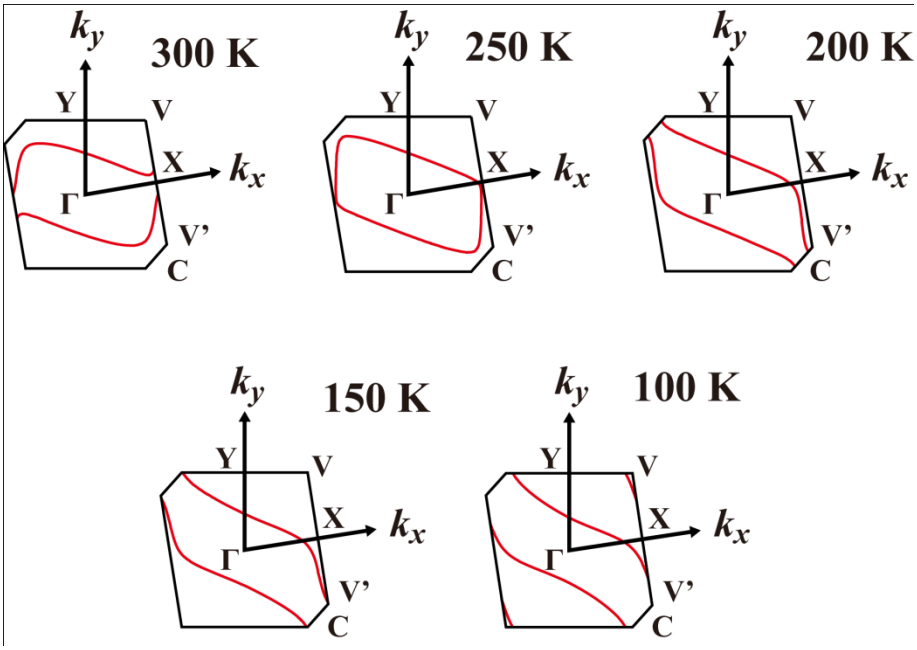

Figure S4 The temperature dependence of the Fermi surface of **1**. The dimensionality of the electronic system (the arrangement of Fermi surface) was determined by the competition between s1 and p1 in Table S4 and was quasi-one dimensional along the inter-columnar interaction (overlap p1) below 200 K.

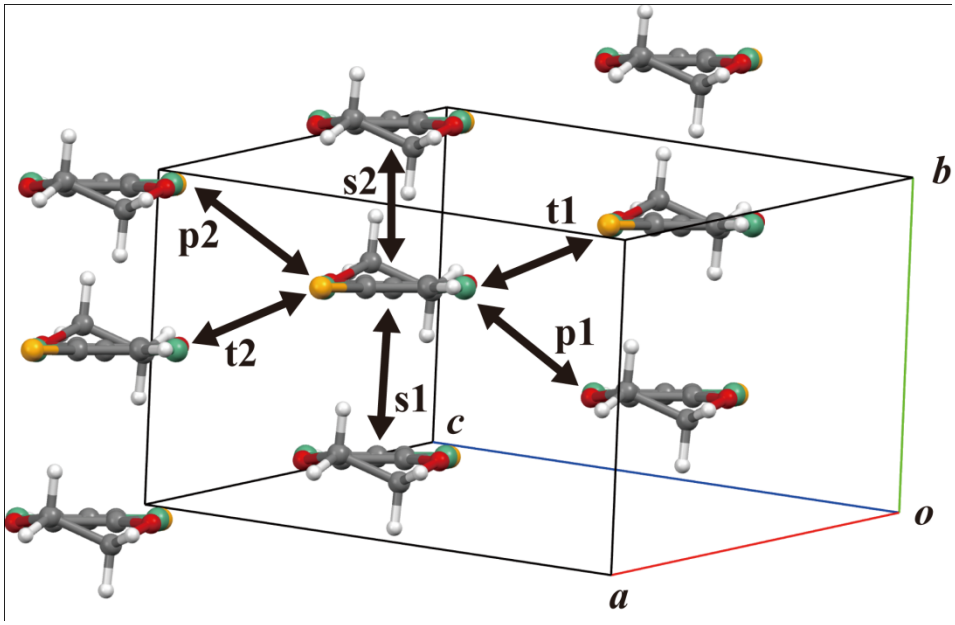

Figure S5 The definition of the overlap integrals in **2** at 300 K.

Table S5. The overlap integrals of $(EDO\text{-}TTF\text{-}Cl)_2SbF_6$ (2) in the unit of 10^{-3}.

Temp.	20 K	100 K	150 K	200 K	250 K	300 K	350 K
s1	25.4	24.9	24.2	23.9	23.7	22.7	21.1
s2	23.2	23.0	22.6	22.9	22.3	21.2	20.4
t1	0.2	0.2	0.1	-0.1	-0.2	-0.3	-0.2
t2	0.2	0.2	0.1	-0.1	-0.2	-0.3	-2.4
p1	6.1	6.1	6.1	6.0	6.2	6.7	7.0
p2	0.6	0.5	0.6	0.7	0.7	0.5	0.5

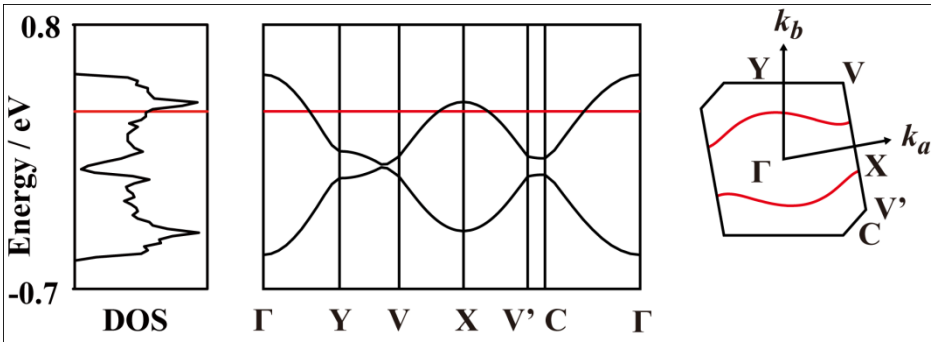

Figure S6 The band structure of **2** at 100 K.

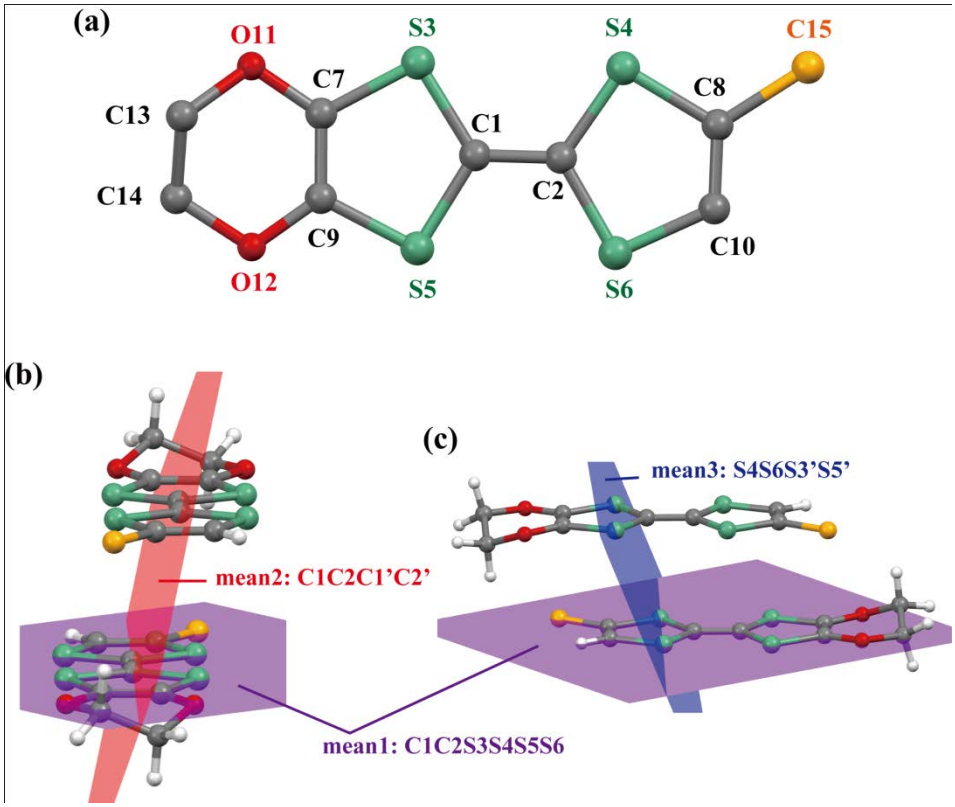

Figure S7 (a) The atomic numbering in the EDO-TTF skeleton for non-hydrogen atoms. (b) and (c) the definition of the mean planes for the estimation of intermolecular displacement d_{short} and d_{long}, respectively. The atomic name used for the mean planes are described besides the mean plane name such as mean2: C1C2C1'C2', where the atoms with prime symbol belong to the neighboring donor to the donor plane (mean1). For example, d_{short} was calculated with the distance between C1 and C1' ($d_{(C1\text{-}C1')}$), the angle for C2-C1-C1' ($\angle$(C2C1C1')), and the dihedral angle between the mean planes 1 and 2 ($\angle$(mean1,mean2)) as $d_{short} = d_{(C1\text{-}C1')}\sin\{\angle(C2C1C1')\}\cos\{\angle(mean1,mean2)\}$. Similarly, d_{long} was calculate by the distance between S4 and S5' ($d_{(S4\text{-}S5')}$), the angle ($\angle$(S4S5S5')), and the dihedral angle ($\angle$(mean1,mean3)) as $d_{long} = d_{(S4\text{-}S5')}\sin\{\angle(S4S5S5')\}\cos\{\angle(mean1,mean3)\}$. The data plotted in Figure 8(b) are the averaged values for possible four pairs of the inter-atomic distances and corresponding angles: C1-C1'($\angle$(C2C1C1')), C1-C2' ($\angle$(C2C1C2')), C2-C1' ($\angle$(C1C2C1')), and C2-C2' ($\angle$(C1C2C2')) for d_{short} and S4-S3' ($\angle$(S4S3S3')), S4-S5' ($\angle$(S4S5S5')), S6-S3' ($\angle$(S6S4S3')), and S6-S5' ($\angle$(S6S4S5')) for d_{long}, respectively.

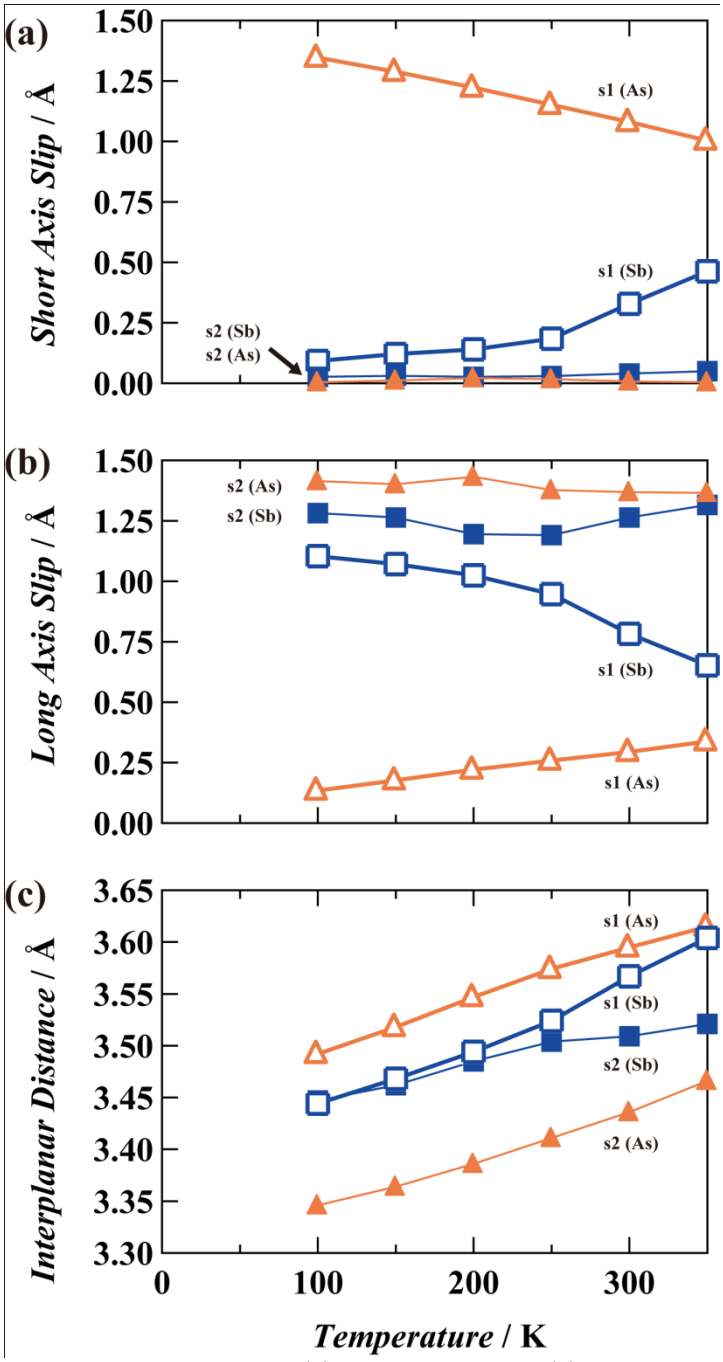

Figure S8 The temperature dependence of the (a) short axis slip, (b) long axis slip, and (c) inter-planar distances for s1 and s2 modes in $(EDO\text{-}TTF\text{-}Cl)_2XF_6$ (X = As, Sb).

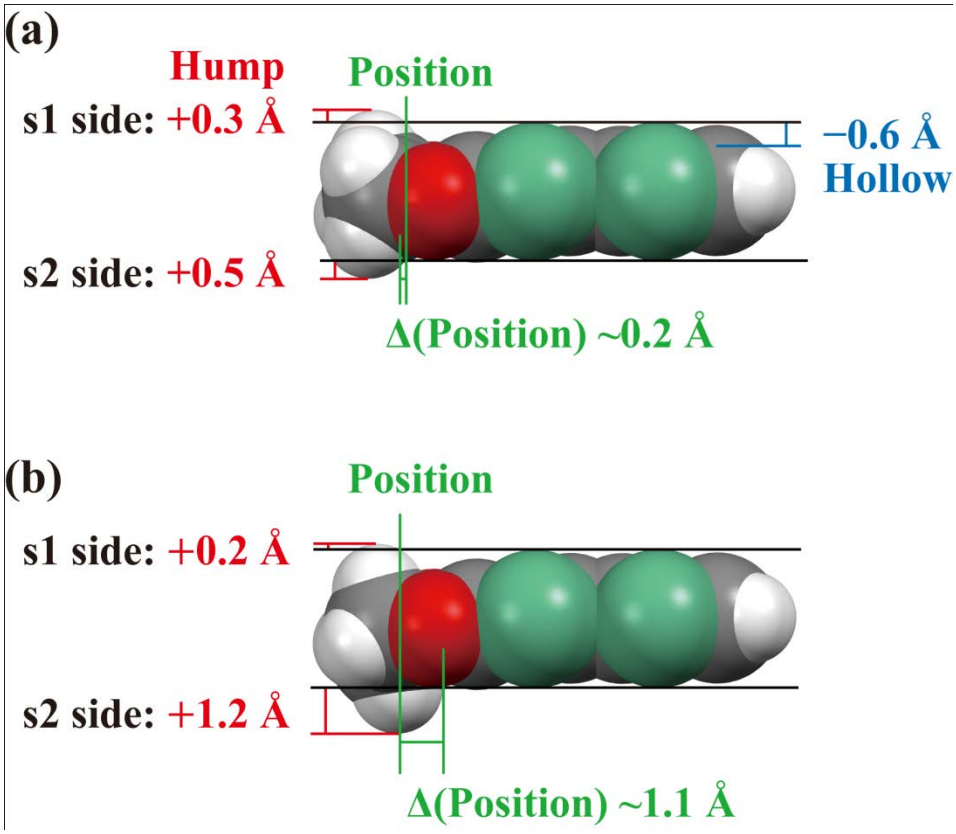

Figure S9 The structural freedom of the ethylenedioxy group in the two disorder patterns (a), (b) in the crystal structure of **3** at 300 K.